Chapter 2
Physical Processes in Optical Emission Spectroscopy

Mario Capitelli, Gianpiero Colonna, Giuliano D'Ammando, Rosalba Gaudiuso and Lucia Daniela Pietanza

Abstract Different aspects of physical processes in optical emission spectroscopy are analyzed in equilibrium and non equilibrium conditions. A very simple but accurate method to calculate the partition function of atomic species based on the reduction of the energy level pattern to a three grouped levels system is introduced. Collisional-radiative models are illustrated with different examples emphasizing the coupling of the electron energy distribution function with excited states population and radiation. Finally, models including fluid dynamic equations to describe the LIBS plume expansion in both one and two space dimensions are discussed, showing that these methods can be used to qualitatively rationalize double pulse experiments and, to some extent, to reproduce experimental results.

2.1 Introduction

Laser Induced Breakdown Spectroscopy (LIBS) diagnostics is currently used in many diagnostic applications, being a candidate either to substitute or to be complementary to Inductively Coupled Plasma (ICP) for some applications, e.g. analysis

M. Capitelli (✉) · G. D'Ammando · R. Gaudiuso
Dipartimento di Chimica, Università di Bari, Via Orabona 4, 70125 Bari, Italy
e-mail: mario.capitelli@ba.imip.cnr.it

G. D'Ammando
e-mail: g.dammando@chimica.uniba.it

R. Gaudiuso
e-mail: rosalba.gaudiuso@ba.imip.cnr.it

G. Colonna · L. D. Pietanza
CNR-IMIP–Sede di Bari, Via Amendola 122/D, 70126 Bari, Italy
e-mail: gianpiero.colonna@ba.imip.cnr.it

L. D. Pietanza
e-mail: daniela.pazienza@ba.imip.cnr.it

S. Musazzi and U. Perini (eds.), *Laser-Induced Breakdown Spectroscopy*,
Springer Series in Optical Sciences 182, DOI: 10.1007/978-3-642-45085-3_2,

of solid samples [1]. The technique is based on the interaction of a laser with a solid surface generating a plasma plume whose emissivity is analyzed to obtain informations on the concentrations of relevant species. LIBS therefore is a diagnostic technique based on Optical Emission Spectroscopy (OES) and as such is similar to any emission spectroscopy including ICP. A major advantage of LIBS over ICP is the extreme simplicity in sample preparation, while both techniques share the same underlying assumption that the formed plasma, due to its high ionization degree, is in a state of Local Thermodynamic Equilibrium (LTE), implying that the Boltzmann plot method can be used to determine the plasma temperature. In LTE, one can also obtain absolute values of the concentration of the different species by measuring the emissivity of a transition. The existence of equilibrium conditions has been used to develop calibration-free LIBS analysis, an attempt which, if successful, will enormously increase the popularity of LIBS technique in analytical chemistry. In this case one can obtain absolute values of the concentration of the different species by measuring the emissivity I_{mn} of a transition in (2.1)

$$I_{mn} = \frac{h\nu_{mn}}{4\pi} A_{mn} N_m \tag{2.1}$$

$$N_m = \frac{N}{Q(T)} g_m e^{-\varepsilon_m/kT} \tag{2.2}$$

where N_m is the density of the atoms or ions in the upper level m, A_{mn} is the Einstein transition probability of $m \rightarrow n$ transition, N is the total number density. $Q(T)$, g_m and ε_m are respectively the atomic partition function, the statistical weight and the energy of the mth level. The absolute measurement of I_{mn} is therefore equivalent to measure N_m as well as of N (the total species density) once the partition function of the different species and the temperature are known. In the common LIBS practice, relative intensities are usually employed and the species concentrations are obtained either with classical calibration techniques [2], or with the Calibration-Free method first proposed in [3] [see also 4]. Through a normalization procedure (the "closure equation") the latter allows obtaining quantitative analyses of major and minor elements (though not of traces) without the use of calibration standards. On the other hand, the calibration-free method relies on the plasma being homogeneous and in LTE, as well as on the accurate knowledge of spectroscopic parameters and of partition functions [5].

The partition function is a tool that every spectroscopist knows and uses, often forgetting the difficulties in obtaining it. In fact in principle the atomic partition function diverges so that a cutoff criterion must be introduced to limit the number of considered energy levels. It is important to remind that the choice of a cutoff criterion introduces a dependence of the partition function on the total density and/or on the electron density. Moreover the common practice of including in the partition function only the observed levels reported in the NIST [6] or Moore tables [7], while obviously avoiding the divergence, results in large errors because of the incompleteness of the relevant level tables (the missing level problem).

These points will be considered in Sect. 2.2 introducing a simplified and accurate treatment of the partition function, the so called three-group model.

Under some circumstances the LIBS plasma cannot be described by equilibrium thermodynamics due to the lack of detailed balance between the direct and inverse elementary processes, implying both non-equilibrium concentrations and non thermal distributions of excited states, where the latter case especially holds true during the high speed expansion of the plasma plume. In this case one should use a kinetic approach named collisional radiative model (CRM) where each atomic electronic state is treated as an independent species submitted to the effect of individual elementary collisional and radiative processes. Due to its enormous practical importance, simple formulae have been proposed to determine the critical electron number density necessary to ensure thermalization of the internal distribution functions. As an example Griem's criterion (valid for hydrogenlike atoms)

$$n_e^* = 7 \times 10^{18} \left(\frac{kT}{E_H}\right)^{1/2} n^{-8.5} \text{ cm}^{-3} \tag{2.3}$$

shows the strong inverse linking between the minimum electron number density n_e^* required for detailed balancing of collisional processes involving a level and the principal quantum number n of the level (E_H is the ionization potential of atomic hydrogen). Other criteria [8–10] are nowadays available, that should however be used with caution because common assumptions made in these equations, i.e. Maxwell distribution function for the free electrons, quasi steady state situations for both electron energy and internal state distributions, homogenous plasma approximation can fail [11, 12] depending on

(a) the temporal regimes where the emission is observed (from fs to ms)
(b) existence of strong spatial gradients during plume expansion.

The first point will be analyzed in Sect. 2.3, where we present time-dependent results of both electron energy distribution functions (eedf) and internal energy distribution functions (iedf) after the laser interaction. No spatial coordinate is considered i.e. eedf and iedf reach stationary values at the given observation point. An open problem is the influence of reabsorption on the population of excited states and eedf, which can be studied introducing the so-called escape probability to approximately model the fact that a fraction of the spontaneously emitted radiation can be unable to escape the local plasma volume due to reabsorption.

The plume expansion, which is the most important characteristic of laser induced breakdown spectroscopy technique, is examined in Sect. 2.4 by means of a fluid-dynamic model based on Euler equations. The plasma expansion can be considered as occurring either in vacuum or against a reactive atmosphere, where the latter can be modeled by an equilibrium chemistry scheme or by the kinetic models described in Sect. 2.3. Part of this section is dedicated to a comparison between experimental and theoretical results, discussing the capability of current models to predict some experimentally observed results, or as a basis for understanding more complicated experiments. Finally Sect. 2.5 reports conclusions and perspectives.

2.2 LTE Plasmas: The Few Level Approximation for the Partition Function and Thermodynamic Properties of Atomic Species

Typical LIBS plasmas, characterized by a dominance of electron impact processes and negligible contribution of radiative losses on the plasma kinetics, are well described by the Local Thermodynamic Equilibrium model (LTE). The LTE model assumes that it is possible to define a local temperature T at each spatial point such that the whole system, made of atoms, ions and electrons, can be fully described through statistical mechanics by defining few parameters, such as the electron, excitation and ionization temperatures and the electron number density. In LTE, species densities follow the well-known Saha-Eggert relation [13] and the iedf and eedf are Boltzmann and Maxwell, respectively, at the same temperature. In an optically thin LTE plasma, (2.1) and (2.2) are valid and can be used to determine the local level population from experimental measurements of emission intensity in atomic lines. A critical quantity entering (2.2) is the atomic partition function $Q(T)$ which depends on the atomic internal electronic states. Other thermodynamic quantities of interest are the internal energy and internal specific heat, needed e.g. in the implementation of fluid-dynamic models of a LIBS experiment. The two main difficulties are the availability of a sufficiently complete set of atomic energy levels for the relevant species, as well as the adoption of a suitable cutoff criterion to eliminate the divergence arising from a strict definition of partition function [see 14 and references therein].

It has been shown [14–16] that accurate atomic partition function values and related thermodynamic functions can be determined with a simplified model including a reduced number of lumped levels. A three-group approximation reads as follows

$$Q(T) = G_0 + G_1 \exp(-\bar{\varepsilon}_1/kT) + G_2 \exp(-\bar{\varepsilon}_2/kT) \tag{2.4}$$

where G_0, G_1 and G_2 are the statistical weights of the ground, first and second lumped levels and $\bar{\varepsilon}_1$ and $\bar{\varepsilon}_2$ corresponding energies referred to the ground lumped level energy. The ground level of the lumped model describes the ground term of the real atom, while the second lumped level represents the low lying states and the last one groups all the other atomic levels. The other thermodynamic functions such as nondimensional internal energy $\widetilde{E} = E/RT$ and nondimensional internal specific heat $\widetilde{C} = C/R$ are calculated using simple analytical expressions [16].

When high accuracy is required, the above formulae can be generalized introducing further lumped levels

$$Q^{(m)}(T) = G_0 + \sum_{i=1}^{m-1} G_i \exp(-\bar{\varepsilon}_i/kT) \tag{2.5}$$

and the other thermodynamic quantities can be consequently calculated [14]

$$\tilde{E}^{(m)} = \frac{\sum_{i=1}^{m-1} G_i(\bar{\varepsilon}_i/kT)\exp(-\bar{\varepsilon}_i/kT)}{Q^{(m)}} \tag{2.6}$$

$$\tilde{C}^{(m)} = \frac{\sum_{i=1}^{m-1} G_i(\bar{\varepsilon}_i/kT)^2\exp(-\bar{\varepsilon}_i/kT)}{Q^{(m)}} - (E^{(m)})^2 \tag{2.7}$$

The statistical weight and energy of the lumped levels are calculated according to

$$G_i = \sum_{\ell\in\mathcal{G}_i} g_\ell \tag{2.8}$$

$$\bar{\varepsilon}_i = \frac{1}{G_i}\sum_{\ell\in\mathcal{G}_i} g_\ell\varepsilon_\ell \tag{2.9}$$

where $\mathcal{G}_i$ is the ith group of atomic levels. To minimize the relative difference between the reduced partition function and the complete one, atomic levels should be grouped according to proximity in energy [15].

As an example let us consider two carbon species C(I)–C(II) (see also [17]). For the low-lying levels, which are critical to obtain good results at low temperature, experimental data must be used. We remark that for the purpose of partition function calculation it is usually sufficient to consider only excited states where a single valence electron is promoted to an higher shell with principal quantum number strictly larger than the valence shell. The energy of these high-lying excited states can be calculated with a simple hydrogenlike formula. With this approximation, the levels used in the lumping procedure are characterized by the integer principal quantum number n only

$$G_i^H = g_{\text{core}}\sum_{n=n_1}^{n_2} 2n^2 \tag{2.10}$$

$$\bar{\varepsilon}_i^H = \frac{g_{\text{core}}}{G_i^H}\sum_{n=n_1}^{n_2} 2n^2\left(I - \frac{\zeta^2 I_H}{n^2}\right) \tag{2.11}$$

where g_{core} is the statistical weight of the atomic term of the ion obtained removing the excited electron, I is the ionization energy of the relevant atom, $\zeta = 1, 2, \ldots$ is the ion charge plus one, I_H is the Rydberg constant and n is the principal quantum number. The finite sums of (2.10) and (2.11) can be analytically evaluated

$$G_i^H = g_{\text{core}}\frac{(n_2 - n_1 + 1)[n_1(2n_1 - 1) + 2n_1n_2 + n_2(2n_2 + 1)]}{3} \tag{2.12}$$

$$\bar{\varepsilon}_i^H = I - \frac{6\zeta^2 I_H}{n_1(2n_1 - 1) + 2n_1n_2 + n_2(2n_2 + 1)} \tag{2.13}$$

n_1 is the principal quantum number of the first shell above the valence shell of the atom, while n_2 depends on the ionization energy lowering ΔI and is calculated from the condition

$$I - \frac{\zeta^2 I_H}{n_2^2} \leq I - \Delta I \Rightarrow n_2 \leq \zeta \sqrt{\frac{I_H}{\Delta I}} \tag{2.14}$$

i.e. we exclude all individual hydrogenlike levels lying above the ionization threshold of the atom reduced by ΔI.

The ground state terms of the C(I) ($2s^2.2p^2(^3P)$) and C(II) ($2s^2.2p(^2P^o)$) species are used to construct the ground lumped level; in this way the reduced partition function will reproduce the low-temperature behavior of the complete one.

C(I) and C(II) have a number of low-lying excited states originating from both spin flips of the valence $2p$ electrons within the same configuration and excitation of one or both the $2s$ electrons to the $2p$ subshell with change of the electronic configuration. Table 2.1 reports the lowest energy rearrangement terms of each carbon ion, where terms used to build the intermediate lumped level for the C(I)–C(II) ion are reported in bold character. The accuracy of the three-level model critically depends on the grouping of these low-lying spectroscopic terms. As a rule, the low-lying spin rearrangement terms should be included, since they dictate the thermodynamic functions at relatively low temperature, when the higher excited states are not yet populated. Higher energy terms can be neglected when their contribution to the thermodynamic functions is overlapped with that of the upper lumped level which, having a much higher statistical weight, makes them negligible.

Let us discuss the application of the above rules to the carbon ions (see Table 2.1). In the case of C(I), the low-lying ^1D and ^1S terms are included in the intermediate lumped level. The ^5S term, with different configuration, is also included in the first excited lumped level since it is very close to the ^1D and ^1S terms and brings a comparatively large statistical weight. On the other hand, the higher energy term $^3D^o$ and $^3P^o$ terms, are neglected since they are sufficiently close to the upper lumped level (with energy close the relevant ionization energy I, Table 2.2) for their effect to be unimportant compared to the latter, even if their total statistical weight is higher than that of the ^1D, ^1S and ^5S terms. The intermediate lumped level of C(II) has been constructed from the ^4P and ^2D terms of $2s.2p^2$ configurations, while higher energy terms can be safely neglected since their total statistical weight is small.

Table 2.2 reports the ionization energy I and the value of g_{core} to be inserted in (2.12) and (2.13) to determine the statistical weight and energy of the upper lumped level of the different ions in the hydrogenlike approximation. These data correspond to the lowest energy ionic term obtained removing the optical electron of C(I)–C(II). The other Rydberg series corresponding to excited core configurations have been neglected due to their small contribution to the partition function compared to the principal series.

Table 2.1 Low-lying terms of the C(I)–C(II) ions

Ion	Configuration	Term	g	Energy [cm^{-1}]
C(I)	$2s^2.2p^2$	**^{1}D**	5	10193.7
		^{1}S	1	21648.4
	$2s.2p^3$	**^{5}S^o**	5	33735.2
		^{3}D^o	15	64088.9
		^{3}P^o	9	75254.9
C(II)	$2s.2p^2$	**^{4}P**	12	43032.3
		^{2}D	10	74931.9
		^{2}S	2	96493.7
		^{2}P	6	110652.0

The terms in bold have been used to construct the first excited lumped level of the three-level model

Table 2.2 Parameters needed for the calculation of the hydrogenlike degeneracy (G_i^H) and energy ($\tilde{\varepsilon}_i^H$) of the second excited lumped level of the three-levels model for C(I)–C(II) ions

Ion	Serie	g_{core}	I [cm^{-1}]
C(I)	$2s^2.2p(^2\text{P}).nx$	6	90878.30
C(II)	$2s^2(^1\text{S}).nx$	1	196659.0

The results of the three-groups model are reported as curves in Fig. 2.1 and compared with accurate reference calculations [18, 19] reported as symbols in the same plots. The upper part of Table 2.3 reports the maximum relative error percentage of the different thermodynamic quantities over the temperature range $1000 \div 50000$ K, using the many-level partition function as reference. The results show a maximum relative error not larger than 10 %. The general trend is an increase of the relative error with ΔI.

The errors reported in Table 2.3 arise from two different sources (a) at low temperature large relative errors are caused by too coarse grouping and/or neglecting of the low-lying terms (b) at large ΔI, deviations of the level energies from the hydrogenlike formula introduce errors in the high temperature part of the reduced partition function.

To understand the impact of the hydrogenlike approximation, thermodynamic quantities have been recomputed using the generalized few-level model of (2.5) using a separate level for all low-lying terms reported in Table 2.1, thus removing the source of error (a). Moreover, it has been shown [15] that grouping of the high-lying excited states does not introduce significant errors, implying that the residual relative error is due to the hydrogenlike approximation only. The relative errors resulting from this improved calculation, reported in the lower part of Table 2.3, show that for $\Delta I \leq 1000$ cm^{-1} the hydrogenlike approximation introduces an error not larger than 3.2 %. The main conclusion is that, at least for not too large ΔI, the hydrogenlike approximation can be used with confidence, eliminating the lengthy procedure of completion of the observed level energy data.

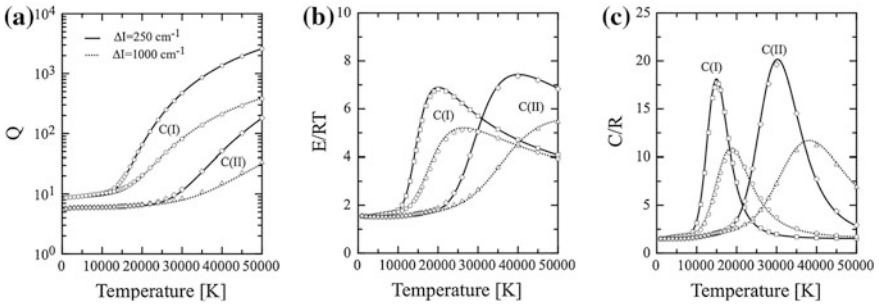

Fig. 2.1 Comparison between (**a**) partition function (**b**) nondimensional internal energy (**c**) nondimensional internal specific heat of C(I)–C(II) calculated using the reduced three-level model (*curves*) or the full partition function (*symbols*), at $\Delta I = 250$ cm^{-1} (*solid lines*) and $\Delta I = 1000$ cm^{-1} (*dotted lines*)

Table 2.3 Maximum relative error in thermodynamic functions at different ΔI for the three-level model, (2.4) (*upper part*) and the generalized few-level model, (2.5) (*lower part*)

	$\Delta I = 250$ cm^{-1}			$\Delta I = 500$ cm^{-1}			$\Delta I = 1000$ cm^{-1}		
	$\delta Q(\%)$	$\delta\widetilde{E}(\%)$	$\delta\widetilde{C}(\%)$	$\delta Q(\%)$	$\delta\widetilde{E}(\%)$	$\delta\widetilde{C}(\%)$	$\delta Q(\%)$	$\delta\widetilde{E}(\%)$	$\delta\widetilde{C}(\%)$
C(I)	7.8	5.2	9.9	8.0	5.2	9.9	8.2	5.2	9.9
C(II)	4.9	3.9	8.0	5.5	4.0	8.0	6.5	4.0	8.0
C(I)	0.68	0.55	1.1	1.5	1.1	2.1	2.4	1.6	3.2
C(II)	0.75	0.53	0.99	1.5	0.98	1.8	2.9	1.7	3.1

2.3 Non-LTE Plasmas: Collisional Radiative Models Coupled with Electron Energy Distribution Function and Radiation Transfer

LIBS plasma are transient and inhomogeneous [20] and if the evolution of the plasma is too fast, the electrons and the atoms could not have time to readjust themselves to new macroscopic conditions and reach thermodynamic equilibrium. In other words, if the expansion time of the plume generated after the laser interaction is smaller or comparable with the time necessary for the population densities of excited states to reach quasi-stationary values, deviations from LTE can occur. In this case, the only way to assess LTE validity is by performing a detailed modeling of LIBS plasma kinetics through a time-dependent Collisional-Radiative model (CRM).

CRM [11, 21–36] consider the processes occurring in a plasma at the kinetic level without invoking the concept of LTE. These models calculate the rate coefficients entering the system of master equation by integrating cross sections over a Maxwell distribution function. Atomic hydrogen, noble gases and more complicated systems have been studied with this approach. The structure of

collisional radiative models starts from the definition of kinetic processes in the plasma. In its simplest formulation, especially valid for hydrogen (or hydrogen-like) atoms merged with their ions and electrons, CRM contains the following processes:

1. electron-impact excitation and de-excitation

$$e^-(\varepsilon) + H(i) \rightleftharpoons e^-(\varepsilon') + H(j) \tag{2.15}$$

2. electron-impact ionization and three-body recombination

$$e^-(\varepsilon) + H(i) \rightleftharpoons e^-(\varepsilon') + H^+ + e^-(\varepsilon_b) \tag{2.16}$$

3. radiative recombination

$$e^-(\varepsilon) + H^+ \rightarrow H(i) + h\nu \tag{2.17}$$

4. spontaneous radiative decay and absorption

$$H(i) \rightarrow H(j) + h\nu_{ij} \tag{2.18}$$

The set of master equations of CRM is represented by the following non-linear system of coupled differential equations, one for each excited state population number density (the subscript in this special case can be identified with the principal quantum number of the ith excited state) and one for the electron and ion density

$$\begin{aligned}\frac{dn_i}{dt} = {} & n_e \sum_{j\neq i} n_j K^e_{ji} - n_i n_e \left(S^e_i + \sum_{j\neq i} K^e_{ij} \right) \\ & + n_{H^+} n_e^2 Q^e_i - n_i \sum_{j<i} A^*_{ij} + \sum_{j>i} A^*_{ji} n_j + n_{H^+} n_e R_i\end{aligned} \tag{2.19}$$

$$\frac{dn_{H^+}}{dt} = \frac{dn_e}{dt} = -n_e n_{H^+} \left(\sum_i R_i + n_e \sum_i Q^e_i \right) + n_e \sum_i S^e_i n_i \tag{2.20}$$

where $A^*_{ij} = A_{ij}\lambda_{ij}$ and A_{ij} are the Einstein coefficients of spontaneous radiative decay (2.18), R_i the rates of radiative recombination (2.17), and K^e_{ij} are, respectively, the rates of electron impact excitation ($i < j$) and de-excitation ($i > j$) (2.15), while S^e_i and Q^e_i are the rates of electron impact ionization and three-body recombination (2.16).

The concept of escape factor is introduced, providing a convenient simplified description of the reabsorption process. The escape factor λ_{ij} of a particular

transition between internal levels i and j, is defined as the probability that an emitted photon with transition frequency ν_{ij} leaves the local plasma volume without being reabsorbed. If A_{ij} is the Einstein coefficient of the transition, the absorption probability can be written as $(1-\lambda_{ij})A_{ij}$. In this way, spontaneous emission and absorption enter the master equation as a single process with an effective rate coefficient given by $A^*_{ij} = \lambda_{ij}A_{ij}$, avoiding an expensive calculation of the radiation field through the solution of a radiative transport equation (RTE).

Electron impact collisions (2.15) and (2.16) drive the excited level distribution towards the Boltzmann distribution, since they fulfill the detailed balance principle [11, 13], which assures that, at equilibrium, the rate of direct and inverse process are equal. On the other hand radiative processes (2.17) and (2.18), lacking of the inverse process in the optically thin case, drive the distribution far from equilibrium.

Rate coefficients for electron-atom collisions are calculated according to

$$K_{ij} = \int_{\varepsilon_{ij}^{tr}}^{\infty} \sigma_{ij}(\varepsilon) f(\varepsilon) v(\varepsilon) d\varepsilon \tag{2.21}$$

where $f(\varepsilon)$ is the eedf, $\sigma_{ij}(\varepsilon)$ the cross section of the transition between atomic levels i and j, $v(\varepsilon)$ the electron velocity and ε and ε_{ij}^{tr} are the electron kinetic energy and threshold energy of the process respectively.

Since times necessary to build up a quasi-stationary eedf are not so short as commonly accepted [11], deviation of eedf from the equilibrium Maxwell distribution can occur during plasma expansion and these deviations can strongly affect the excited level distribution. In order to model a non-equilibrium eedf, the electron Boltzmann equation (BE) must be solved self-consistently with the system of kinetic equations. In the homogeneous, time-dependent and quasi-isotropic case, the BE can be written in the following compact form [37–39]

$$\frac{\partial f(\varepsilon,t)}{\partial t} = \frac{\partial J_E}{\partial \varepsilon} - \frac{\partial J_{el}}{\partial \varepsilon} - \frac{\partial J_{e-e}}{\partial \varepsilon} + S_{\text{in}} + S_{\text{sup}} \tag{2.22}$$

where the J terms are the fluxes in the electron energy space due to the electric field (J_E), elastic electron-atom (J_{el}) and electron–electron (J_{e-e}) collisions, while the S terms are the sources due to inelastic (S_{in}) and superelastic (S_{sup}) collisions. Inelastic collisions are the electron impact excitation and ionization, forward processes in (2.15), and (2.16), while superelastic collisions are electron impact de-excitation and recombination, inverse processes in (2.15) and (2.16).

The system of master (2.19) and (2.20) and the BE (2.22) are strongly coupled: electron impact rate coefficients (2.21) are calculated from the eedf, while the J and S terms depend on plasma composition as well as on isdf. Thus (2.19), (2.20) and (2.22) should be solved simultaneously and self-consistently.

To solve them we must introduce an initial condition for the different variables. As an example, we consider the case of an (H, H^+, e^-) plasma submitted to a sudden cooling, resulting in a recombination regime. Hydrogen plasmas are not typical LIBS plasmas, mostly because LIBS plasmas are generated by the

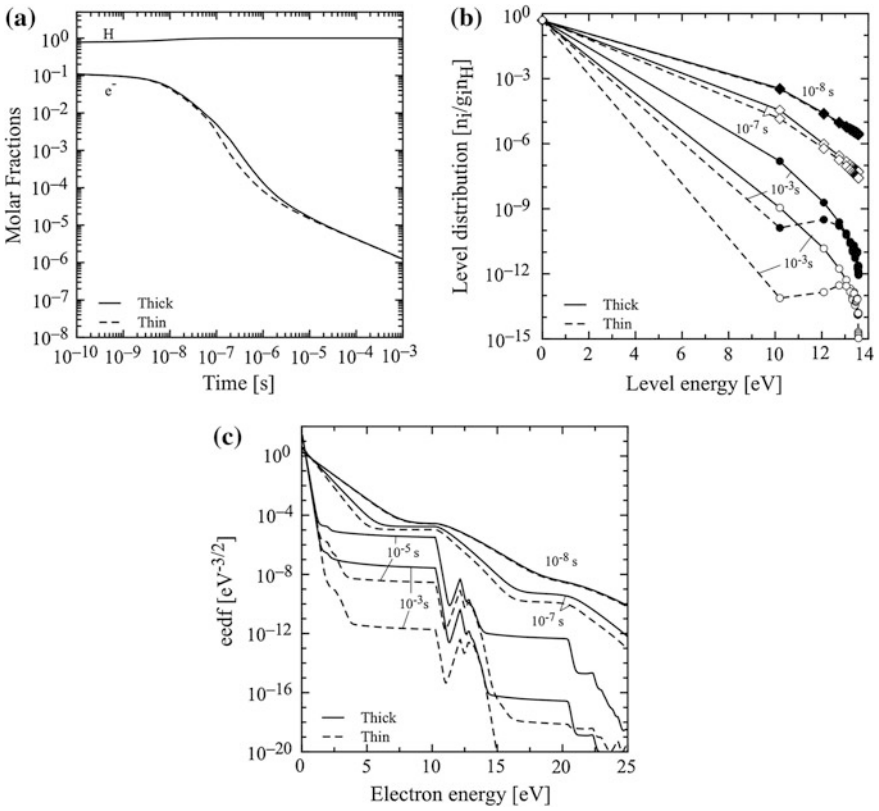

Fig. 2.2 Time evolution of (**a**) composition (**b**) isdf of H atom (**c**) eedf in a recombining hydrogen plasma under the following initial conditions: $T_e = T_H = 15,000$ K, $T_g = 1000$ K and $ID_0 = 0.1$ at $p = 1$ atm. Optically thick (*solid line*) and optically thin (*dashed line*) result are reported

interaction of a laser with a solid target, a condition which can be met for hydrogen only at extreme conditions. However, once the gaseous plasma is formed, its general behavior does not strongly depend on the chosen system. For the recombining plasma, the initial ionization degree (ID_0) is put equal to 0.1, while the internal distribution of excited $H(i)$ levels is a Boltzmann at $T_H = T_e =$ 15000 K and eedf is a Maxwell–Boltzmann distribution at the same electron temperature T_e. The plasma is suddenly cooled at $T_g = 1000$ K and both eedf and iedf start relaxing. The two limit cases of thin ($\lambda_{ij} = 1$) and thick ($\lambda_{ij} = 0$) plasmas are compared in Fig. 2.2a–c.

Before examining the results we want to briefly illustrate the general behavior of both iedf and eedf expected for this case. First of all we expect a strong cooling of the eedf through elastic and inelastic collisions with atoms leading, at very long times, to the relaxation of the eedf to a Maxwell distribution at the gas temperature T_g. Moreover we can expect a strong decrease of the electron density and a

consequent decrease of the concentration of electronically excited states. Low electron temperature and low ionization degrees are the ideal conditions for the action of the second kind (superelastic) collisions which tend to transport low energy electrons to high energy through the processes

$$H(2) + e^-(\varepsilon) \rightarrow H(1) + e^-(\varepsilon + \varepsilon_{12}), \quad \varepsilon_{12} \approx 10.2 \text{ eV} \tag{2.23}$$

and

$$H(3) + e^-(\varepsilon) \rightarrow H(1) + e^-(\varepsilon + \varepsilon_{13}), \quad \varepsilon_{13} \approx 12.1 \text{ eV} \tag{2.24}$$

and so on for higher n-values. These processes depend on the concentration of excited states which is higher in the thick plasma case.

These observations are recovered in the Fig. 2.2a–c. Inspection of Fig. 2.2a shows the strong decrease of the electron density in the recombination regime: small differences are observed for the two cases i.e. thin and thick plasmas. On the other hand the concentration of atomic hydrogen does not practically change also due to neglecting of the molecular hydrogen formation, which can be important for $t > 10^{-5}$ s in the reported results.

Figure 2.2b reports the normalized concentration of excited atomic hydrogen at different times. We can see that at $t = 10^{-8}$ s no differences are observed for thin and thick case, the two distributions reflect the initial situation. For $t > 10^{-7}$ s large differences appear in the concentration of excited states for the two cases; as an example the concentration of the first excited state at $t = 10^{-5}$ s for the thick case is about three orders of magnitude higher than the corresponding concentration of the thin case. The differences are smaller for $n = 3$, becoming negligible for $n > 3$. This behavior is a consequence of the fact that electron collision rates overcome radiative rates for higher excited states, following the trend of the corresponding cross sections. The temporal behavior of excited states associated to the decrease of electron density and therefore of their thermalizing action on eedf through Coulomb collisions is responsible of the time evolution of eedf.

Figure 2.2c compares the eedf for thin and thick conditions at increasing times. We can see that the two situations start giving different results already at $t = 10^{-7}$ s, the differences becoming extremely important from 10^{-5} s on. In this last case the eedf presents a very low temperature as can be appreciated by looking at the eedf for $\varepsilon < 3$ eV, thus magnifying the role of second kind collisions. The long plateaux existing in both thin and thick cases are due to the initial build-up of a peak in the eedf at $\varepsilon = 10.2$ eV followed by redistribution through elastic (including electron–electron) and inelastic collisions. The differences in the two cases are due to corresponding differences in the concentration of the first excited state of H atom. From $t = 10^{-5}$ s on additional superelastic peaks in eedf, due to the second kind collisions from the second and the third excited state of atomic hydrogen, start appearing. In this case the differences between the thin and thick cases are less important due correspondingly smaller differences in the number densities of these higher excited states. It should be also noted that second kind

collisions act also at early times, i.e. 10^{-8} s, despite the initial large electron concentration.

In [40] a CRM approach has been used to study an optically thin laser-generated aluminium plasma (Al, Al^+, Al^{++}, e^-), comparing with experimental excitation temperatures and total density measured in [41]. To determine reasonable initial conditions required to simulate the expansion of the aluminum plasma in air background, the following assumptions have been made

1. the time profile of T_{gas} has been constructed scaling the experimental internal temperature profile reported in [41]. to give the best agreement between experimental and calculated ionization degree.
2. for the time profile of N_{tot} the experimental data have been directly used.
3. the initial ionization degree has been fixed to $ID_0 = 0.997$, compatible with an almost complete ionization of the laser-induced plasma.

The internal distributions of Al and Al^+ follow the Boltzmann function and the eedf the Maxwell distribution, as a consequence of fact that the ionization degree keeps very high values during the entire temporal evolution, ensuring a dominance of electron collisions and a fast thermalization of distributions, and implying completely different conditions from those studied in the hydrogen example. However, even if the distributions are equilibrium, the associated temperatures are not equilibrated as can be observed in Fig. 2.3, which reports the time evolution of gas, electron and excitation temperatures. T_e, T_{0-1}^{Al} and $T_{0-1}^{Al^+}$ equilibrate only for $t > 10^{-10}$ s and are in any case different from the gas temperature [40].

Figure 2.4 shows a comparison of calculated ionization degree and heavy particle excitation temperatures with experimental data (see [41]) in the temporal range 200–2200 ns. As can be observed, the ionization degree predicted by the CRM follows the experimental profile, with theoretical values slightly below the experimental ones. The discrepancy could be due either to the Kramers [42] approximation used to compute radiative recombination cross sections, that could overestimate the plasma recombination or to the scaled T_g profile (which strongly affects the ionization degree) that could be underestimating the actual one [40]. A much better agreement is found between the theoretical and experimental excitation temperatures, demonstrating the validity of the proposed CRM method applied LIBS plasmas.

Going beyond the escape factor approach, a self-consistent treatment of radiation reabsorption can only be achieved at the cost of solving a radiative transport equation (RTE) to determine the spatial distribution of the photon density. For example, in a simple one-dimensional setting the following non-scattering, axisymmetric radiative transfer equation (RTE) in slab geometry [43] must be solved

$$\mu \frac{\partial I_\nu(x,\mu)}{\partial x} = j_\nu^e(x) + \kappa_\nu'(x) I_\nu(x,\mu) \tag{2.25}$$

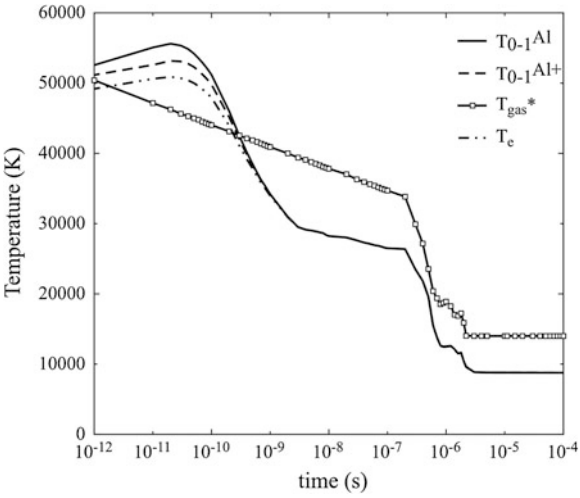

Fig. 2.3 Time evolution of gas temperature (T_{gas}), electron (T_e) and excitation heavy particle Al and Al^+ (T_{0-1}^{Al} and $T_{0-1}^{Al^+}$) temperatures calculated by a CRM self-consistently coupled with the BE for in an aluminium plasma (Al, Al^+, Al^{++}, e^-) with a time-varying gas temperature and pressure according experimental data in [40]

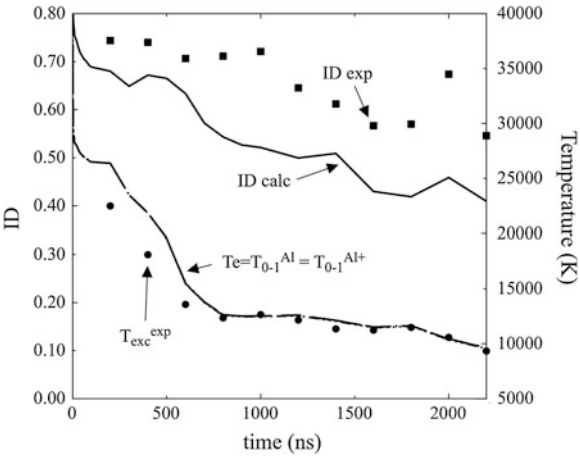

Fig. 2.4 Comparison between experimental (*squares*) and calculated (*lines*) ionization degree (*left axis*) and between experimental excitation temperature (*circles*) and calculated ones, T_{0-1}^{Al} and $T_{0-1}^{Al^+}$, for an aluminium plasma. The experimental data have been taken from [41]

where $I_\nu(x, \mu)$ is the radiation intensity propagating along a ray with director cosine μ with respect to the x-axis. The term $j_\nu^e(x)$ is the spectral emissivity, $\kappa_\nu'(x)$ is the absorption coefficient corrected for stimulated emission.

Once the RTE has been solved, the angular average of the spectral intensity can be calculated

$$J_\nu(x) = \frac{1}{2}\int_{-1}^{1} I_\nu(x, \mu) d\mu \tag{2.26}$$

The net rate of a bound–bound transition between atomic levels i and j, taking into account the radiation field, is calculated as

$$\left(\frac{dn_j}{dt}\right)_{ij} = -\left(\frac{dn_i}{dt}\right)_{ij} = -[A_{ji} + B_{ji}\bar{J}_{ij}]n_j + B_{ij}\bar{J}_{ij}n_i \tag{2.27}$$

where

$$\bar{J}_{ij} = \bar{J}_{ji} = \int_0^\infty J_\nu(x)\phi_{ij}(\nu)\,d\nu \tag{2.28}$$

and $\phi_{ij}(\nu)$ is the normalized line profile associated to the $i \leftrightarrow j$ transition. The master equation system (2.19) can be rewritten as follows

$$\begin{aligned}\frac{dn_i}{dt} = {} & n_e \sum_{j\neq i} n_j K^e_{ji} - n_i n_e \left(S^e_i + \sum_{j\neq i} K^e_{ij}\right) \\ & + n_{H^+} n_e^2 Q^e_i - n_i \left[\sum_{j<i}(A_{ij} + B_{ij}\bar{J}_{ij}) + \sum_{j>i} B_{ij}\bar{J}_{ij}\right] \\ & + \sum_{j>i} n_j (A_{ji} + B_{ji}\bar{J}_{ij}) + \sum_{j<i} n_j B_{ji}\bar{J}_{ij} + n_{H^+} n_e R_i\end{aligned} \tag{2.29}$$

Since the $J_\nu(x)$ depends on the number densities though the absorption coefficient and emissivity, the above equation introduces a non-linear dependence between the local populations and those of nearby points that affect radiation reaching the current point. This non-linearity is handled by alternating the solution the system (2.29) and of (2.25) until convergence of the level populations is achieved. An application of the above fully self-consistent method to a simplified 1D shock wave model can be found in [44, 45].

2.4 Fluid Dynamics of Laser-Plasma Expansion in Gas and Liquids: Modeling and Validation

Spatial and temporal evolution of Laser-Induced Plasmas (LIPs) in background environment involves a large ensemble of phenomena, thus combined efforts between theoretical models and experimental data are required for its interpretation. Models of the LIPs expansion are based on Euler equations. To model the expansion of a plume produced by a laser pulse we solve the Euler equations [46–51]

$$\begin{aligned}&\frac{\partial \rho}{\partial t} + \nabla \cdot \rho u = z_d \\ &\frac{\partial \rho u}{\partial t} + \nabla \cdot u(\rho u) + \nabla P = z_u \\ &\frac{\partial \rho \varepsilon}{\partial t} + \nabla \cdot u\varepsilon + P\nabla \cdot u = z_e\end{aligned} \tag{2.30}$$

where ρ is the mass density, $\vec{u}$ is the flow speed, ε is the energy per unit mass and P is the gas pressure. The z's are the source terms for the production of matter,

momentum and energy. In our case these terms account for the surface evaporation due to the laser pulse. The source term z_e can be modified to consider also the absorption of the photons in the gas and the energy loss due to emission.

Euler equations must be closed with additional conditions and in particular:

1. the equation of state, that, as a first approximation can be the one of ideal gases ($\bar{m}$ is the mean molar mass)

$$P = \frac{\rho RT}{\bar{m}} \tag{2.31}$$

2. an equation for the energy that in general can be written as

$$\epsilon = \frac{1}{2}u^2 + \varepsilon_{int} \tag{2.32}$$

where ε_{int} is the internal energy. The expression of this last contribution depends on the chemistry model. In equilibrium conditions it depends only on the gas temperature (see Sect. 2.2), in chemical non-equilibrium conditions it depends on the gas composition and gas temperature, more in general, it depends on composition and on internal distributions (see Sect. 2.3). Therefore, to calculate the internal energy, it is necessary to model a multi-component reacting flow, i.e. we have to add a continuity equation for each species *s*th in each level *l*th as

$$\frac{\partial \rho_{sl}}{\partial t} + \nabla \cdot \rho_{sl} u = z_{d,sl} \tag{2.33}$$

with the condition

$$\sum_{sl} \rho_{sl} = \rho \qquad \sum_{sl} z_{d,sl} = z_d \tag{2.34}$$

The z source terms in (2.30) and (2.33) include also the production of matter due to the surface evaporation. To model the ablation stage, we have used a heuristic approach [48], fitting the experimental *time of flight* (TOF).

From the experimental point of view, time-resolved optical emission spectroscopy and spectrally-resolved imaging are important techniques for the study of processes occurring in LIPs, both from the microscopic point of view (i.e., determination of number densities of the species in the plasma and of the degree of ionization) and the macroscopic one (i.e., observation of the expansion dynamics of the plasma and of its interaction with the background) [52–55]. Spectroscopic data can be complemented with other optical techniques, which can provide useful information about phenomena accompanying the evolution of LIPs. For example, the formation and evolution of cavitation bubbles associated to the decay of LIPs in aqueous environment can be studied through shadowgraph [56 and references therein], while the production of nanoparticles by laser ablation in liquids can be followed with laser scattering techniques [56, 57].

The temporal evolution of LIPs is characterized by the transition through different stages, that can be related to the changes of plasma number density (decreasing from $\approx 10^{22}$ to $\approx 10^{16}$ cm^{-1} during the plasma lifetime). Analogously, deep changes are observed in the plasma dynamics during expansion in different background environments, and can be interpreted as well in terms of different plasma number densities.

Figure 2.5a–e gives an overview of the plasma evolution in media of different state of aggregation, pressure and chemical nature. Here, emission spectra of Ti plasmas induced by single and multiple laser pulses in air at atmospheric pressure, air at reduced pressure and liquid water are reported at different delays after the end of the laser pulse.

The spectra of Fig. 2.5 allow two main observations to emerge very clearly. First, the plasma lifetime (or persistence) is strongly dependent on the background environment, being of the order of few hundreds of nanoseconds in water and in air at reduced pressure, and of microseconds in gaseous background at atmospheric pressure, be it air or water vapor in the cavitation bubble (see later on for a description of the formation of laser-induced cavitation bubbles). Second, the use of multiple laser pulses with optimized interpulse delays produces deep modifications in the emission spectra, particularly in the case of plasma production in an aqueous background which suggests that plasma dynamics must be affected as well. The qualitative observations reported above can be complemented, on a more quantitative basis, by Fig. 2.6, that displays the maxima of emission intensity spatial distributions of Ti LIPs in different experimental conditions plotted as functions of time. These intensity distributions were obtained through spectrally and space-resolved images, and virtually represent the expansion profile of LIPs in different environments.

As can be inferred from Fig. 2.6, the plasma expansion in vacuum is very fast, thus causing the plasma number density and the electron density to fall down to values of the order of 10^{16} cm^{-3}. In turn, lower electron density implies limited Stark broadening and radiative recombination, which renders spectral lines thin and well resolved and the continuum background low and short-lived (see Fig. 2.5e), but leads as well to short plasma persistence and possible deviations from LTE. These issues are both consequences of the faster dynamics of plasmas produced in vacuum and of the lack of confinement by the background gas, and become as more severe upon decreasing the background pressure, as the typical expansion timescale approaches that of recombination (10^{-7} s) and electron density values fall below those indicated by the McWhirter criterion. On the other hand, slightly sub-atmospheric pressure could be an optimal choice for analytical LIBS, in that they could offer a suitable compromise between expansion dynamics compatible with LTE, and moderate plasma confinement from the ambient gas. At the same time, possible complications from a strong chemical/physical interaction of the plasma with the background could be avoided and the duration of the continuum in the spectra reduced [56, and references therein]. Other typical features of LIPs in reduced pressure environment, well documented in the PLD

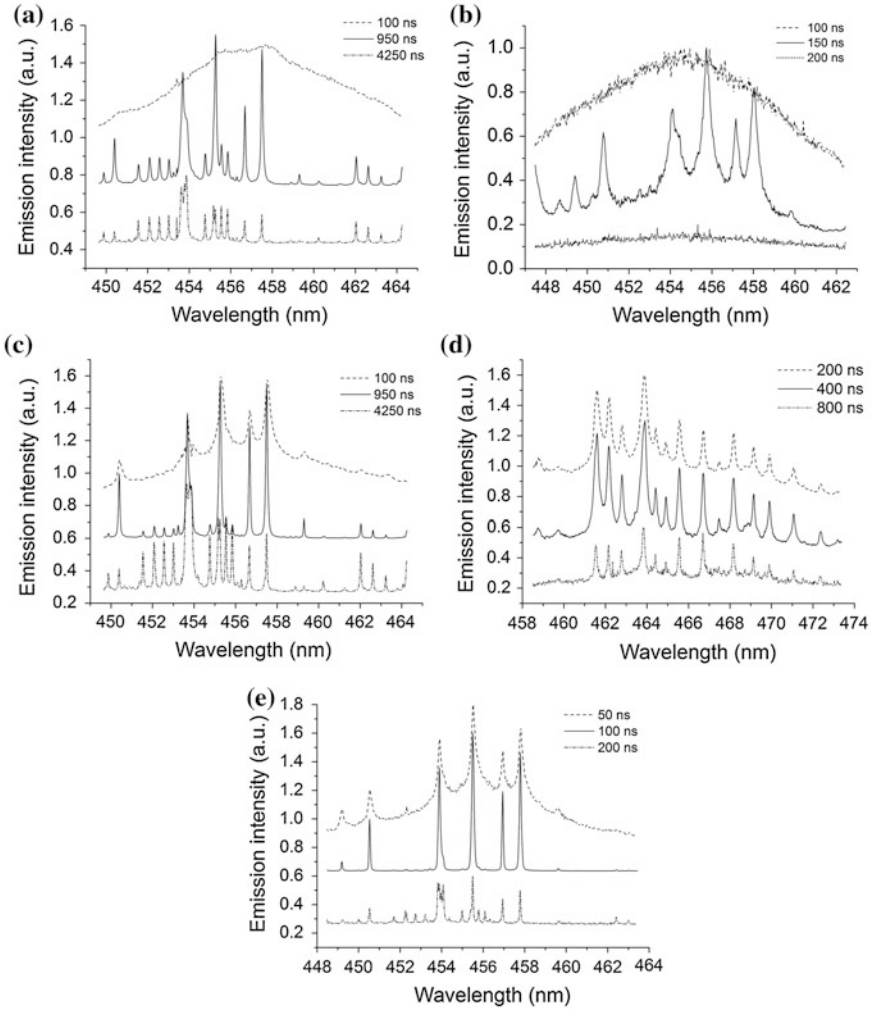

Fig. 2.5 (**a**)–(**e**) Time evolution of Ti emission spectra in different background environment and experimental conditions: (**a**) Single Pulse (SP) in air, (**b**) SP in water, (**c**) DP in air at optimized interpulse delay 5 μs, (**d**) Double Pulse (DP) in water at optimized interpulse delay 100 μs, (**e**) SP in air 9 Pa. The spectra are intensity-shifted for the sake of figure readability

literature, are their strongly directional expansion, virtually orthogonal to the target direction with no components in the radial direction [58] and the lack of chemical interaction with the background gas. From a modeling point of view, this implies that 1D models are adequate for describing the plume dynamics [58–60]. This is demonstrated very clearly by Fig. 2.7, which shows an excellent agreement between experimental and theoretical profiles of emission intensity of atomic and ionic species in a Ti LIP expanding in vacuum.

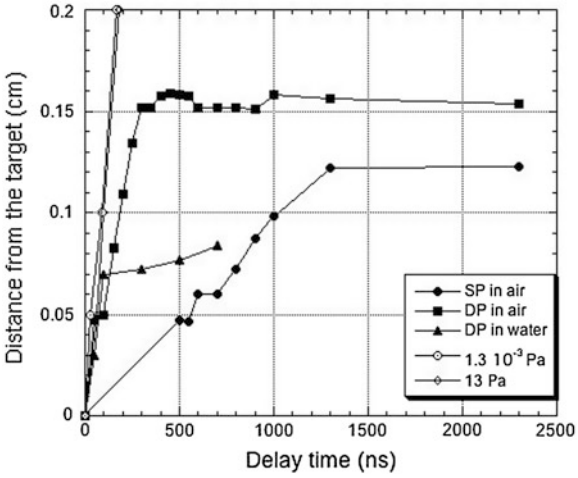

Fig. 2.6 Maxima of Ti II emission intensity distribution as a function of time, during the ns-laser ablation of a Ti target at different experimental conditions [73]

On the other hand, in high-pressure ambient, i.e. gas/vapour at atmospheric pressure and water, the expansion symmetry of the plume becomes virtually spherical and 1D models tend to overestimate the flow speed, though they still remain very useful for a qualitative description. In these conditions, 2D models can be developed to take into account the confinement effect experienced by the plume, and its fluid-dynamic and chemical consequences.

In air atmospheric pressure (where LIBS experiments are most commonly performed) the plasma expansion is accompanied by the formation of shock waves: an external shock wave, propagating outward, is driven in the background gas; an internal shock wave, formed by the backscattered material, is reflected back and forth between the sample surface and the plasma/external shockwave contact wall, until it degrades to a sound wave ($\approx$ 100 ns after the end of the laser pulse) and the gas behind the contact wall homogenizes [61–63]. Thus the plasma expands against the background air and is confined by the shock front, inducing dissociation, ionization and excitation of nitrogen and oxygen molecules, and having its expansion braked by the ambient gas. Few microseconds later, upon reaching the gas-dynamic equilibrium with the environment, the plasma virtually stops expanding. From the spectral point of view, this causes the spectra to change as shown in Fig. 2.5a: at short delays they feature a broad continuum due to radiative recombination and high-density effects limiting the number of accessible levels; at longer delays the radiative energy loss is negligible and the spectra consist of well resolved emission peaks due to ionic (at shorter delays) and atomic (at longer delays) transitions.

Good qualitative agreement is again obtained between experiments and models for what concerns the description of the expansion of a Ti LIP in air in reduced and atmospheric pressure. In Fig. 2.8 results of a 2D model simulation are reported for Ti LIPs expanding in background air at two different pressures, 1 and 10^{-3} atm.

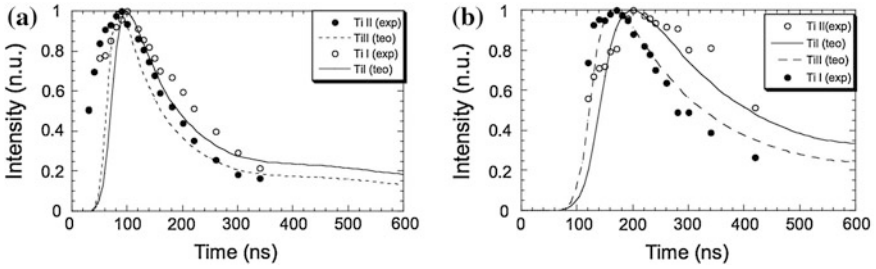

Fig. 2.7 Comparison between experimental and calculated TOF at 1 mm (*left*) and 2 mm (*right*)

The theoretical mixture density profiles shown in Fig. 2.8 compare well with experimental observations obtained from emission spectra reported in Fig. 2.5a and e and from spectrally resolved images. In particular, the temporal distributions of plasma intensity given in Fig. 2.6 give a piece of information directly comparable to the theoretical one, showing clearly the higher degree of plasma confinement experienced at atmospheric pressure than in vacuum. Clearly, the formation of LIPs in liquid environment stands at the far end with respect to rarefied gaseous background. Though LIBS experiments have been performed in various liquids, including solvents and molten metals, salts and glasses [64, and reference therein], water remains the most studied, due to the capital importance that laser medicine has been acquiring in the last decades [62, 65]. In water, the whole picture of laser-induced breakdown is made more complicated by many additional phenomena, including non-linear effects, electron hydration, laser filamentation and white light generation, coherent scattering, beam self-focusing, medium heating and production of quasi-free electrons by photolysis [see 66, and references therein]. Not surprisingly, experimental evidence shows clearly that when produced in bulk water or at the surface of a submerged target, the plasma undergoes much more pronounced interaction with the surrounding environment, loosing most of its internal energy in dissociating and evaporating water, as well as being compressed by water itself. This causes it to extinguish within few hundreds of nanoseconds and, due to enhanced radiative recombination, to emit mostly continuum spectra and very broadened lines (if any), as can be observed in Fig. 2.5b. Both in air and in water, the use of multiple pulses induces deep modifications in the plasma dynamics and, consequently, in the emission spectra. In the analytical LIBS literature, Double Pulse (DP) experiments are carried out with the main purpose of enhancing the signal intensity and plasma stability and persistence [67, 68]. Several experimental configurations have been investigated to this end, but in the following only the geometry with two collinear laser beams will be addressed. In this configuration, as in the orthogonal one with a pre-spark [69], the role of the first pulse is to produce a suitable environment for the expansion of the plasma produced by the second pulse. In water, this involves the vaporization of the liquid layers adjacent to the decaying first plasma and the formation of a laser-induced cavitation bubble in the liquid bulk. The bubble expands and

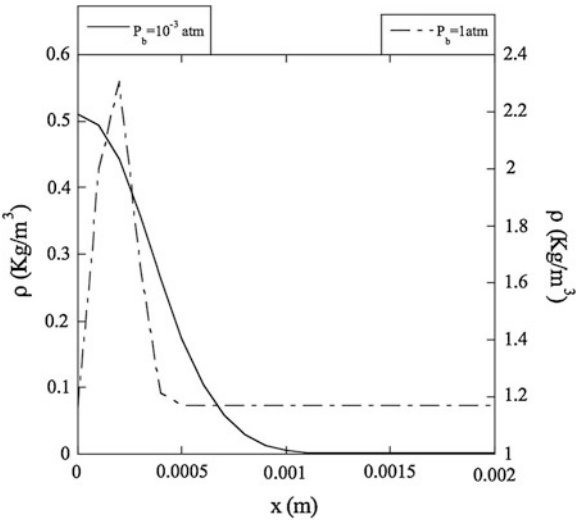

Fig. 2.8 Mixture density profile as a function of distance from the target after 5×10^{-8} s from the beginning of the laser pulse along the normal in the middle of the target. The expansion occurs in air background at 10^{-3} atm (on the *left*) and 1 atm (*right*)

collapses with oscillation period of the order of 10^2 μs, as shown by Fig. 2.9, where are reported several shadowgraph frames acquired during the time evolution of a laser-induced cavitation bubble formed at the surface of a submerged Ti target. Thanks to its much longer lifetime than the plasma's, the cavitation bubble can be considered as an almost stationary environment where the second plasma can be formed, by shooting the second laser pulse at the desired interpulse delay, and expand in a gaseous background. An appropriate choice of the interpulse delay is essential to optimize pressure and temperature of the vapor in the bubble, which represents in this case the background environment for the second plasma. In Fig. 2.10 are shown Double Pulse (DP) LIBS spectra taken at different interpulse delays. At short interpulse delays (700 ns, 10 μs), i.e. at the beginning of the bubble expansion, pressure and temperature of the water vapour are such as to reproduce confinement conditions analogous to those of the single pulse plasma, produced directly in water. The situation is similar at long interpulse delays, i.e. close to the bubble collapse (140, 160 μs). On the other hand, at intermediate interpulse delays, corresponding to the maximum bubble expansion, well-resolved spectra can be obtained, and the evolution of the plasma in the bubble is similar to that in background air at atmospheric pressure, as depicted in Fig. 2.5d.

In air the choice of the interpulse delay is less critical, though different phenomena can occur by changing it. At short interpulse delay, direct coupling between the second laser pulse and the first plasma can take place, while very long interpulse delay would form two separate non-interacting plasmas. At optimized interpulse delays, emission intensity and plasma persistence increase, due to the different degree of interaction with the background environment of the SP and DP plasmas, and thus to their different expansion dynamics [68]. This difference is shown clearly in Fig. 2.6: while the SP plasma (i.e., in a DP experiment, the first

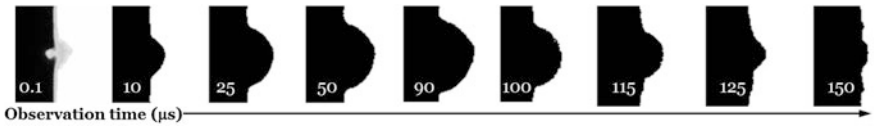

Fig. 2.9 Time-resolved shadowgraph images of the laser induced bubble on Ti target submerged in water (laser fluence = 68 J/cm^2, gate width = 5 μs)

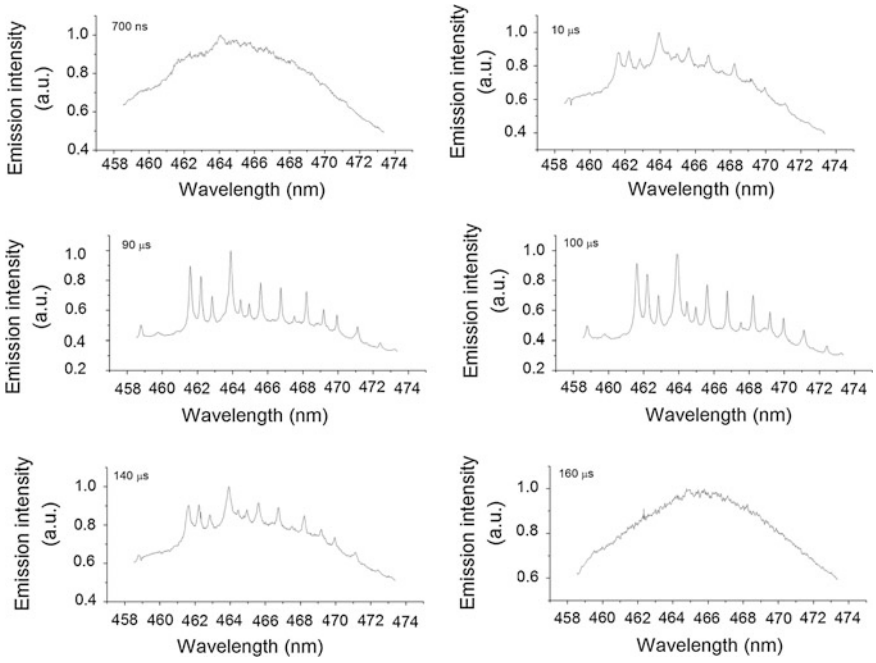

Fig. 2.10 DP-LIBS emission spectra of Ti in water at different interpulse delays (Nd:YAG 7 ns ablation lasers; 1st pulse fluence 0.51 J/cm^2, 2nd pulse fluence 6 J/cm^2)

pulse plasma) is confined and has its expansion braked by the surrounding air, the DP one (i.e., the second pulse plasma) expands in a more favorable environment, namely the late first pulse plasma, which is still confined behind the first laser-induced shock wave. Thus, the second pulse plasma expands faster, reaching the contact wall, bouncing and expanding in the backward direction (see the profile shown in Fig. 2.6. Since the second pulse plasma is virtually prevented from directly interacting with the background air, fewer ion–electron recombination events take place, and chemical reactions with oxygen and nitrogen molecules are avoided. Consequences on the emission spectra cannot be easily appreciated comparing the spectra shown in Fig. 2.5b and d, but are very clear upon acquisition and analysis of spectrally resolved images [68]. The result is longer plasma

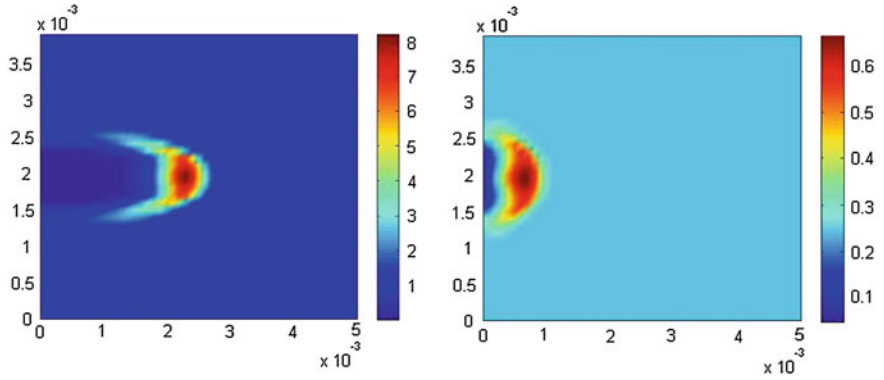

Fig. 2.11 Two-dimensional density profile after 1×10^{-7} s from the beginning of the laser pulse. Comparison between air background (*left*) and water vapour background (*right*)

persistence, higher ionization degree, shorter intensity and duration of the continuum radiation, and lack of signals from molecular and atomic air species.

The role of chemical reactions between the plume and the background molecules is pictured efficiently in Fig. 2.11. This shows a comparison between theoretical density profiles obtained with a 2D model in air (a) and in water vapour (b), both at atmospheric pressure. The latter situation is achieved in experiments of LIBS in a cavitation bubble, namely, in DP-LIBS in water with interpulse delay corresponding to the maximum of cavitation bubble expansion, when the water vapour pressure in the bubble approaches the atmospheric one [66].

In [70] it was shown that introducing chemical reactions in the model causes the flow to decelerate with respect to the free flow case, because the conversion of kinetic energy in chemical energy of the surrounding molecules is taken into account. The density profiles reported in Fig. 2.11 indicate that in water vapour the plume is slower and displays much more pronounced radial broadening than in air. This in turn implies that the confinement effect and the amount of translational energy spent in chemical interactions are higher, consistently with the higher chemical reactivity of water with respect to nitrogen and oxygen molecules.

2.5 Conclusions and Perspectives

Physical aspects of LIBS plasmas have been discussed in this chapter considering both equilibrium and non equilibrium situations. For the equilibrium case we have proposed a simple method to calculate the partition function of atomic species based on the reduction of the energy level pattern to a three lumped level system. This model is found to give results in good agreement with those of complete partition functions including a complete set of atomic energy levels. The method provides a

practical approach to compute tables of partition functions to be used in optical spectroscopy, in particular for the development of calibration-free LIBS analysis.

Non-equilibrium problems have been considered both from the point of view of kinetics and of fluid dynamics. Collisional-radiative models are discussed with particular emphasis on the coupling of the eedf with the excited state kinetics, including also the effect of radiative reabsorption. This coupling, which is due to superelastic collisions of electronically excited states and cold electrons, is such to create structures in eedf which are enhanced in the case of strong reabsorption of radiation, which in turn increases the concentration of excited states. A CRM has also been used to rationalize experimental results in LIBS Al plasmas, even though in this case the coupling between eedf and kinetics of excited states is hidden by the high ionization degree characterizing the experimental plasma.

We have introduced theoretical tools that can be used to study the temporal evolution of the LIBS plasma plume in both one- and two-dimensional situations. These methods are in general valuable to qualitatively rationalize double pulse experiments and in some cases also to quantitatively reproduce experimental results. A limitation of the present two-dimensional Euler model is that it considers equilibrium chemistry instead of a more sophisticated state-specific kinetic model.

The present results, even though still far from a realistic description of a LIBS plasma, can be further improved to achieve a better understanding of the plume dynamics. In particular, for femtosecond LIBS technique [71], the models can be improved by inserting in the 2D fluid dynamics a self-consistent collisional radiative model coupled to the kinetics of electronically excited states as well as to a radiative transfer model. The radiative module is needed to eliminate the empirical escape factors used to account for radiation reabsorption in our collisional radiative model. In any case the present approach opens new perspectives for the interpretation of LIBS plasmas, especially considering that, in parallel to the creation of sophisticated kinetic models, an increasing number of accurate collisional cross sections and radiative data needed by the models are becoming available thanks to the improvement in both numerical methods and computer power.

Finally, one should develop 2D Navier–Stokes models to go beyond the limitations of the Euler equations especially in modeling the plume evolution at relatively large delay times [72]. These improvements are necessary to create predictive numerical tools which can then be validated with the advanced experimental techniques already operating in our laboratory.

Acknowledgments The research leading to these results has received funding from the European Community Seventh Framework Programme (FP7/2007–2013) under grant agreement n. 242311 and from Regione Puglia under INNOVHEAD, avviso Miur n. 713/Ric. The LIBS experimental group (A. De Giacomo, O. De Pascale, M. Dell'Aglio, G. Senesi) and A. Casavola are acknowledged for the useful discussions and for providing results.

References

1. F. Capitelli, F. Colao, M.R. Provenzano, R. Fantoni, G. Brunetti, N. Senesi, Geoderma **106**(1–2), 45 (2002)
2. R. Fantoni, L. Caneve, F. Colao, L. Fornarini, V. Lazic, V. Spizzichino, Spectrochim. Acta, Part B **63**(10), 1097 (2008)
3. A. Ciucci, M. Corsi, V. Palleschi, S. Rastrelli, A. Salvetti, E. Tognoni, Appl. Spectroscop. **53**(8), 960 (1999)
4. E. Tognoni, G. Cristoforetti, S. Legnaioli, V. Palleschi, Spectrochim. Acta, Part B **61**(1), 1 (2010)
5. E. Tognoni, G. Cristoforetti, S. Legnaioli, V. Palleschi, A. Salvetti, M. Mueller, U. Panne, I. Gornushkin, Spectrochim. Acta, Part B **62**(12), 1287 (2007)
6. NIST, Technical report (2009), http://www.nist.gov/
7. C.E. Moore, Selected tables of atomic spectra. Nbs-467 (National Bureau of Standards, Washington, D. C, 1949)
8. H.W. Drawin, Zeitschrift für Physik **228**, 99 (1969)
9. R.W.P. McWhirter, *Plasma Diagnostic Techniques* (Academic Press, New York, 1965), Chap. 5, pp. 201–264
10. G. Cristoforetti, A. De Giacomo, M. Dell'Aglio, S. Legnaioli, E. Tognoni, V. Palleschi, N. Omenetto, Spectrochim. Acta, Part B **65**(1), 86 (2010)
11. M. Capitelli, G. Colonna, M. Catella, F. Capitelli, A. Eletskii, Chem. Phys. Lett. **316**(5–6), 517 (2000)
12. M. Capitelli, F. Capitelli, A. Eletskii, Spectrochim. Acta, Part B **55**(6), 559 (2000)
13. M. Mitchner, C.H. Kruger, *Partially Ionized Gases* (John Wiley & Sons, New York, 1973)
14. M. Capitelli, G. Colonna, A. D'Angola, *Fundamental Aspects of Plasma Chemical Physics: Thermodynamics* (Springer, New York, 2012)
15. G. Colonna, M. Capitelli, Spectrochim. Acta, Part B **64**(9), 863 (2009)
16. G. D'Ammando, G. Colonna, L.D. Pietanza, M. Capitelli, Spectrochim. Acta, Part B **65**(8), 603 (2010)
17. G. D'Ammando, G. Colonna, M. Capitelli, Phys. Plasmas **20**, 032108 (2013)
18. M. Capitelli, G. Colonna, D. Giordano, L. Marraffa, A. Casavola, P. Minnelli, D. Pagano, L.D. Pietanza, F. Taccogna, Tables of internal partition functions and thermodynamic properties of high-temperature mars-atmosphere. Technical report STR-246, European space agency (2005)
19. M. Capitelli, G. Colonna, D. Giordano, L. Marraffa, A. Casavola, P. Minnelli, D. Pagano, L.D. Pietanza, F. Taccogna, J. Spacecrafts and Rockets **42**(6), 980 (2005)
20. T. Fujimoto, *Plasma Spectroscopy*. The International Series of Monographs on Physics (Oxford University Press, Oxford, 2004)
21. D.R. Bates, A.E. Kingston, R.W.P. McWhirter, P. Roy, Soc. Lond. A Mat. **270**(1341), 155 (1962)
22. D.R. Bates, A.E. Kingston, R.W.P. McWhirter, P. Roy, Soc. Lond. A Mat. **267**(1330), 297 (1962)
23. C.C. Limbaugh, A.A. Mason, Phys. Rev. A **4**, 2368 (1971)
24. M. Cacciatore, M. Capitelli, Z. Naturforsch. **30**, 48 (1975)
25. M. Cacciatore, M. Capitelli, J. Quant. Spectrosc. Ra. **16**, 325 (1976)
26. C. Gorse, M. Cacciatore, M. Capitelli, Z. Naturforsch. **33**, 895 (1978)
27. J.A. Kunc, W.H. Soon, Phys. Rev. A **40**, 5822 (1989)
28. W.H. Soon, J.A. Kunc, Phys. Rev. A **41**, 825 (1990)
29. K. Sawada, T. Fujimoto, Phys. Rev. E **49**, 5565 (1994)
30. J. Vlcek, Spectrochim. Acta, Part B **5**, 599 (1997)
31. A. Bogaerts, R. Gijbels, R.J. Carman, Spectrochim. Acta, Part B **53**(12), 1679 (1998)
32. A. Bogaerts, R. Gijbels, J. Vlcek, J. Appl. Phys. **84**, 121 (1998)
33. J. Van Der Mullen, J. Jonkers, Spectrochim. Acta, Part B **7**, 1017 (1999)

34. P. Teulet, J.P. Sarrette, A.M. Gomes, J. Quant. Spectrosc. Ra. **70**, 159 (2001)
35. M. Goto, J. Quant. Spectrosc. Ra. **76**(3–4), 331 (2003)
36. C.P. Balance, D.C. Griffin, S.D. Loch, R.F. Boivin, M.S. Pindzola, Phys. Rev. A **74**, 012719 (2006)
37. G. Colonna, M. Capitelli, J. Thermophys. Heat Transfer **22**, 414 (2008)
38. C.J. Elliot, A.E. Greene, J. Appl. Phys. **47**, 2946 (1976)
39. S.D. Rockwood, Phys. Rev. Lett. **8**, 2348 (1973)
40. L.D. Pietanza, G. Colonna, A. De Giacomo, M. Capitelli, Spectrochim. Acta, Part B **65**(8), 616 (2010)
41. A. De Giacomo, M. Dell'Aglio, D. Bruno, R. Gaudiuso, O. De Pascale, Spectrochimica Acta Part B **63**(7), 805 (2008)
42. Y.B. Zel'dovich, Y.P. Raizer, *Physics of Shock Waves and High-Temperature Hydrodynamic Phenomena* (Dover Publications, New York, 2002)
43. A. Peraiah, *An Introduction to Radiative Transfer: Methods and Applications in Astrophysics* (Cambridge University Press, Cambridge, 2007)
44. G. Colonna, L.D. Pietanza, G. D'Ammando, Chem. Phys. **398**, 37–45 (2012)
45. M. Capitelli, G. Colonna, L.D. Pietanza, G. D'Ammando, Spectrochim. Acta, Part B (83–84), 1–13 (2013)
46. M. Capitelli, A. Casavola, G. Colonna, A. De Giacomo, Spectrochim. Acta, Part B **59**(3), 271 (2004)
47. A. Casavola, G. Colonna, A. De Giacomo, O. De Pascale, M. Capitelli, Appl. Opt. **42**(30), 5963 (2003). doi:10.1364/AO.42.005963
48. A. Casavola, G. Colonna, M. Capitelli, Appl. Surf. Sci. **208**, 85 (2003)
49. A. Casavola, G. Colonna, A. De Giacomo, M. Capitelli, J. Thermophys. Heat Transfer **17**(2), 225 (2003). doi:10.2514/2.6755
50. Appl. Phys. A: Mater. Sci. Process. 79(4–6), 1315 (2004)
51. G. Colonna, A. Casavola, M. Capitelli, Proc. SPIE **4070**, 293–299 (2000)
52. S. Amoruso, B. Toftmann, J. Schou, R. Velotta, X. Wang, Thin Solid Films **453–454**, 562 (2004)
53. C. Aragón, J.A. Aguilera, Spectrochim. Acta, Part B **63**, 893 (2008)
54. H. Hahn, N. Omenetto, Appl. Spectroscop. **64**, 335A (2010)
55. L.J. Radziemski, D.A. Cremers, *Laser-induced plasma and applications* (Marcel Dekker, New York, 1989)
56. A. Casavola, A. De Giacomo, M. Dell'Aglio, F. Taccogna, G. Colonna, O. De Pascale, S. Longo, Spectrochim. Acta, Part B **60**, 975 (2005)
57. A. De Giacomo, M. Dell'Aglio, A. Santagata, R. Gaudiuso, O. De Pascale, P. Wagener, G.C. Messina, G. Compagnini, S. Barcikowski, Phys. Chem. Chem. Phys. (2012)
58. D.B. Chrisey, G.K. Hubler, *Pulsed Laser Deposition of Thin Films* (John Wiley & sons, New York, 1994)
59. S. Amoruso, Appl. Phys. A: Solids Surf. **69**, 323 (1999)
60. R. Kelly, Phys. Rev. A **46**, 860 (1992)
61. N. Arnold, J. Gruber, J. Heitz, Appl. Phys. A: Solids Surf. 69 [Suppl], S87 (1999)
62. S. Wen, X. Mao, R. Greif, R.E. Russo, J. Appl. Phys. **101**, 023115 (2007)
63. S. Wen, X. Mao, R. Greif, R.E. Russo, J. Appl. Phys. **101**, 023114 (2007)
64. J.P. Singh, S.N. Thakur, *Laser-Induced Breakdown Spectroscopy* (Elsevier, Amsterdam, 2007)
65. P.D. Kennedy, D.X. Hammer, B.A. Rockwell, Prog. Quantum Electron. **21**, 155 (1997)
66. A. De Giacomo, M. Dell'Aglio, O. De Pascale, M. Capitelli, Spectrochim. Acta, Part B **62**, 721–738 (2007)
67. V.I. Babushok, D.F.C. Jr, J.L. Gottfried, C.A. Munson, A.W. Miziolek, Spectrochim. Acta, Part B **61**, 999 (2006)
68. A. De Giacomo, M. Dell'Aglio, D. Bruno, R. Gaudiuso, O. De Pascale, Spectrochim. Acta, Part B **63**, 805 (2008)
69. J. Scaffidi, S.M. Angel, D.A. Cremers, Anal. Chem. **78**, 24 (2006)

70. A. Casavola, G. Colonna, A. Cristofolini, C.A. Borghi, M. Capitelli, J. Thermophys. Heat Transfer **22**, 407 (2008)
71. T.B. Petrova, H.D. Ladouceur, A.P. Baronavski, Phys. Plasmas **15**(5), 053501 (2008)
72. H.C. Le, D.E. Zeitoun, J.D. Parisse, Phys. Rev. E **62**, 4152 (2000)
73. A. De Giacomo, M. Dell'Aglio, R. Gaudiuso, S.S. Amoruso, O. De Pascale, Spectrochim. Acta, Part B **78**, 1 (2012)

http://www.springer.com/978-3-642-45084-6

Laser-Induced Breakdown Spectroscopy
Theory and Applications
Musazzi, S.; Perini, U. (Eds.)
2014, XXII, 565 p. 244 illus., 34 illus. in color., Hardcover
ISBN: 978-3-642-45084-6